



Remote Monitoring of Civil Infrastructure Based on TomoSAR

Alessandra Budillon ^{1,2,*} and Gilda Schirinzi ^{1,2}

¹ Dipartimento di Ingegneria, Università di Napoli "Parthenope", 80143 Napoli, Italy; gilda.schirinzi@uniparthenope.it

² Consorzio Nazionale Interuniversitario per le Telecomunicazioni (CNIT), 43124 Parma, Italy

* Correspondence: alessandra.budillon@uniparthenope.it

Abstract: Structural health monitoring and damage detection tools are extremely important topics nowadays with the civil infrastructure aging and deteriorating problems observed in urban areas. These tasks can be done by visual inspection and by using traditional in situ methods, such as leveling or using traditional mechanical and electrical sensors, but these approaches are costly, labor-intensive and cannot be performed with a high temporal frequency. In recent years, remote sensing has proved to be a very promising methodology in evaluating the health of a structure by assessing its deformation and thermal dilation. The satellite-based Synthetic Aperture Radar Tomography (TomoSAR) technique, based on the exploitation of a stack of multi-temporal SAR images, allows to remotely sense the movement and the thermal dilation of individual structures with a centimeter-to millimeter-level accuracy, thanks to new generation high-resolution satellite-borne sensors. In this paper, the effectiveness of a recently developed TomoSAR technique in assessing both possible deformations and the thermal dilation evolution of man-made structures is shown. The results obtained using X-band SAR data in two case studies, concerning two urban structures in the city of Naples (Italy), are presented.



Citation: Budillon, A.; Schirinzi, G. Remote Monitoring of Civil Infrastructure Based on TomoSAR. *Infrastructures* **2022**, *7*, 52. <https://doi.org/10.3390/infrastructures7040052>

Academic Editors: Carlo Rainieri, Giovanni Fabbrocino, Filippo Santucci de Magistris and Matilde Antonella Notarangelo

Received: 7 March 2022

Accepted: 4 April 2022

Published: 6 April 2022

Publisher's Note: MDPI stays neutral with regard to jurisdictional claims in published maps and institutional affiliations.



Copyright: © 2022 by the authors. Licensee MDPI, Basel, Switzerland. This article is an open access article distributed under the terms and conditions of the Creative Commons Attribution (CC BY) license (<https://creativecommons.org/licenses/by/4.0/>).

Keywords: civil infrastructure monitoring; structure health monitoring; remote sensing; SAR; tomography; generalized likelihood ratio test

1. Introduction

Structure health monitoring (SHM) [1] consists in the stability monitoring of man-made structures such as buildings, highways, and bridges, that suffer from deterioration, aging, inadequate upkeep or earthquake damage. Monitoring civil infrastructure allows to detect the deformation at an early stage, preventing risks and keeping public safety and quality of life. Timely inspections of civil infrastructures usually involve human resources, in situ contact sensor, and considerable funds. Contact sensors are characterized by high sensitivity and can monitor the most critical points of the constructions, detecting factors that may be symptoms of poor structural health, such as anomalous displacements. Temperature structure monitoring and the resultant strain and displacement is another structural health tool (Temperature Driven-Structural Health Monitoring or TD-SHM) [2,3]. Changes in the signatures that describe the structure's behavior with temperature indicate unusual behavior or damage. A fundamental parameter for this analysis is the Coefficient of Thermal Expansion (CTE), which is the amount of expansion or contraction a material undergoes per degree change in temperature.

A solution for the routine inspections of civil infrastructures with reduced human resources and affordable costs is based on remote sensing systems, such as synthetic aperture radar (SAR), that offer the possibility for large area and millimeter-level surface deformation monitoring under all day and during all weather conditions [4,5].

In particular, synthetic aperture radar interferometry (InSAR) is a cost-effective methodology for measuring surface deformation over large areas [3–6]. By applying multi-temporal InSAR processing techniques, (for example Persistent Scatterers PS InSAR) [7–10] to a series

of SAR images acquired during time over the same region, it is possible to detect the line of sight (LOS) movements of ground and of civil infrastructures, and to evaluate the average velocity of their movements with a millimeter sensitivity. Therefore, it is possible to detect anomalous movements indicating potential stability structure problems that require further ground investigations. An early problem detection allows to mitigate their impact on structural health. Different sensors can be used for frequently monitoring a specific area of interest. For instance, ERS, Envisat, and Radarsat have monthly revisit time, while Sentinel, TerraSAR-X, and COSMO-SkyMed provide even weekly revisit time [11,12]. Moreover, it is also possible to map deformations which occurred in the past, if images of the site were acquired. Several studies have highlighted the potential of PS InSAR techniques in estimating the displacement of civil structures and of their thermally induced displacement that exhibits a seasonal behavior [13]. PS InSAR techniques are essentially phase model-based and assume the presence of one dominant scatterer within a resolution cell [7–13]: the deformation is measured only over the available coherent pixels. The deformation model usually cannot be assumed linear, especially in the case of civil structures, such as bridges, railways, and specific buildings with metallic cover, whose construction materials may be sensitive to thermal dilation effects. In this case, due to the temperature changes, the structure may undergo large non-linear seasonal deformations [14]. In general, the interferometric phase is modeled as the sum of deformation, thermal dilation effect, and noise terms. In order to measure the deformation contribution, which is independent of temperature variations, the estimation of the thermal dilation contribution is crucial [15,16]. Recently, based on conventional InSAR, various time-series InSAR techniques have been developed, aimed at mapping and characterizing the thermal dilation of different infrastructure types [17–19]. The magnitude of thermal dilation is proven to be highly variable for each infrastructure since it is associated with the material properties and sizes of the objects [19]. In general, it achieves values of the order of millimeter. The capability to measure thermal dilation contribution is related to sensor sensitivity, in particular, sensors in X-Band, such as TerraSAR-X and the Italian COSMO-SkyMed constellation, characterized by a very small wavelength (~ 3.1 cm), allows to measure small surface displacements, even those caused by thermal dilation of the imaged targets.

Even if PS InSAR techniques are widely used in this field, they undergo two-fold limitations when monitoring specific structures in urban areas: on one side, the phase unwrapping operation [4] (the complex-valued phase interferogram is modulo 2π and must be unwrapped) in correspondence of many height discontinuities can be inaccurate, and, on the other side, the assumption of only single scatterer in the resolution cell cannot allow to consider the layover problem [20]. Layover is a geometric distortion present inside the looking radar: in the illuminated scene, the echoes from multiple scatterers at different height, but at the same slant range, are summed up, and contribute to the same resolution cell, ending up in a brighter area in the SAR image. This phenomenon can impair the selection of PS and the corresponding height and displacement estimation.

This limitation can be overcome using SAR tomography (TomoSAR) [20–22] where scatterers interfering within the same range-azimuth resolution cell are separated by synthesizing apertures along the elevation direction. In study [21], it has been shown that the number of scatterers detected using TomoSAR is higher than that identified by PS-InSAR. In structure health monitoring, a higher detected point density allows, on one side, to better identify the critical points that need to be monitored, and on the other side, to infer with more accuracy potential damage for the structure monitored if the point cloud exhibits the same anomalous deformation behavior. The higher scatterer density in the TomoSAR case is due to the coherent processing of the complex valued data (amplitude and phase) in the elevation direction, that allows to increase the signal to clutter ratio in the focused 3D domain. InSAR techniques, instead, are based on only-phase data. Moreover, in TomoSAR, the estimation of the scatterers' parameters is performed by simultaneously exploiting all the acquisitions, thus allowing an optimal smoothing of the phase noise and of the additive clutter effect, with a subsequent increase of the estimation accuracy.

TomoSAR is still based on a stack of SAR images acquired at different times but considers both amplitude and phase of the acquired signals and allows to provide the full 3D scene reflectivity profile along azimuth, range, and elevation. Moreover, it does not require the phase unwrapping but mainly consists in resolving a spectral estimation problem. Different spectral estimators have been proposed, such as Singular Value Decomposition (SVD) [23] and Compressive Sensing (CS) [24–26].

TomoSAR techniques derive the elevation and deformation parameters of multiple scatterers present in each resolution cell, together with noise contributions and artifacts that can be misinterpreted as scatterers. One of the main issues that must be faced is the correct detection of true scatterers in presence of noise and outliers. This problem can be treated by fixing the maximum number of scatterers that can be present in each resolution cell and using a detector [27], based on a statistical model of the data, capable of detecting the presence of scatterers and estimating their number. The detector proposed in [27] is based on a sequential Generalized Likelihood Ratio Test (GLRT), which allows to detect the presence of single and double scatterers, controlling the number of outliers with an assigned false alarm rate. The detection performance depends also on the number of measurements and on the signal to noise ratio (SNR).

In study [28–30], different GLRT approaches have been proposed, achieving super resolution capabilities. This is a very important issue in urban structures monitoring for discriminating scatterers which are very close in elevation, such as those coming from the building roof, façade and ground, or from different height buildings in the same illuminated area.

Extended phase models [31–35] have been introduced to allow simultaneous retrieval of scatterer elevation (3D map) and of deformation parameters, with the generation of a 4D map, by adding the velocity deformation contribution [33], and 5D map, adding the thermal dilation effect [34].

The Multi-look GLRT (MGLRT) [36] has been introduced for the detection and monitoring of weak scatterers at close-to-full resolution in urban areas. It achieves an improved detection efficiency of PSs with constant false alarm rates compared with single-look GLRT approaches [28,29].

In this paper, the results obtained by using the MGLRT TomoSAR technique based on the extended phase model [36,37], in order to retrieve the 5D reconstruction of buildings in urban areas, are presented. Multi-looking operation essentially involves an averaging operation on the signals acquired in a given neighborhood of each range-azimuth image pixel, for reducing the noise effect and improving the result accuracy. Anyway, two considerations have to be made:

1. the averaging operation produces a reduction of the range and azimuth resolutions, which can impair the reconstruction of small and medium-sized structures;
2. for achieving a good performance, the averaging operation has to be performed over an area that is spatially stationary (without elevation changes), otherwise it can lead to results that are worse than the ones obtained in the single-look case.

It follows that for structure monitoring in urban areas, where a high spatial resolution is required, and the observed scene is not spatially stationary, a multi-looking operation has to involve a very small number of pixels.

Results on real TerraSAR-X (TSX) data are presented in order to investigate if TomoSAR techniques can be used for assessing both possible deformations and thermal dilation evolution of man-made structures. The results obtained using X-band SAR data in two case studies, concerning two urban structures in the city of Naples (Italy), are presented.

To sum up, the main contributions of the paper are:

1. Showing the potential of TomoSAR as a structure health monitoring technique:
 - a. on real TSX data, starting from unfiltered single-look complex SAR images;
 - b. on small-size urban infrastructure, where it is crucial to detect, as much as possible, scatterers providing reliable results.

considering a linear and a nonlinear contribution: a slow linear contribution, in time, with a mean velocity, that models a linear land subsidence phenomenon; a nonlinear contribution in time but linear in temperature, that models the material thermal dilation, and a limited nonlinear contribution that is neglected. Following these assumptions, the LOS deformation [31,34] is:

$$d(s, t_m, T_m) = v(s)t_m + k(s)T_m + d_{NL}(s, t_m, T_m), \tag{2}$$

where T_m is the temperature of the scene at the time t_m , $v(s)$ is the mean velocity of the slow linear deformation, having the dimension of (m/sec), and $k(s)$ is the coefficient of thermal dilation, having the dimension of (m/°C), of the scatterer at elevation s , representing the phase to temperature sensitivity, and depending upon material and/or physical structure.

Typically, as reported in the Introduction, the thermal deformation component is of the order of mm/°C and can be estimated thanks to the X-Band sensors, that allow a higher phase sensitivity to range variations with respect to other C or L-Band sensors.

The coefficient of thermal dilation k in Equation (2) is given by $k = \Delta L / \Delta T$, where ΔL is the change in length of the solid structure due to a change in temperature ΔT . It is related to the Coefficient of linear Thermal Expansion (CTE) α of the solid structure, that represents the percentage variation in length per degree of temperature (m/(m·°C)), by the relation $k = \alpha L_0$, where L_0 is the initial length of the given solid [38].

We note that in Equation (2), a simple thermal expansion model, linear with temperature, has been assumed; indeed, the civil structures are not thermally uniform, and undergo a more complex thermally induced displacement that depends on the geometry, the construction material, and the temperatures across the entire structure. A more sophisticated model will certainly ensure better thermal dilation estimates, but this is not the aim of the paper. We aim to show the potential of a TomoSAR technique in the field of civil structure monitoring and the need to include the thermal expansion in the adopted phase model. Even considering a linear model, the inclusion of the thermal contribution allows to achieve more accurate height and deformation estimates.

In the case of urban areas, most of the elevation profiles are sparse, i.e., they consist only of a few discrete scatterers, for instance, in Figure 1, three contributions (A, B, C) in the same (r - x) cell are considered. In this paper, we focalize on structures to be monitored and on high reliable points positioned on them; for this reason, we search for a dominant coherent scatterer in each (r - x) cell, but applying a TomoSAR technique, we exploit both amplitude and phase signals and avoid the unwrapping operation, which can be critical when observing areas with highly discontinuous height profiles, as happens in urban areas.

Discretizing Equation (1), we can assume a signal model in two different hypotheses: presence of a target (H_1) or absence of a target (H_0):

$$\begin{aligned} \mathbf{u} &= \mathbf{w} & H_0 \\ \mathbf{u} &= \mathbf{a}(s, v, k)\gamma + \mathbf{w} & H_1 \end{aligned} \tag{3}$$

with

$$\begin{aligned} \mathbf{u} &= [u(b_1) \quad u(b_2) \quad \dots \quad u(b_M)]^T \\ \mathbf{w} &= [w(b_1) \quad w(b_2) \quad \dots \quad w(b_M)]^T \\ \mathbf{a}(s, v, k) &= \left[e^{j(\frac{4\pi b_1}{\lambda R_0} s + \frac{4\pi t_1}{\lambda} v + \frac{4\pi T_1}{\lambda} k)} \quad e^{j(\frac{4\pi b_2}{\lambda R_0} s + \frac{4\pi t_2}{\lambda} v + \frac{4\pi T_2}{\lambda} k)} \quad \dots \quad e^{j(\frac{4\pi b_M}{\lambda R_0} s + \frac{4\pi t_M}{\lambda} v + \frac{4\pi T_M}{\lambda} k)} \right]^T \end{aligned} \tag{4}$$

where g is the reflectivity coefficient of the dominant coherent scatterer present in the r - x cell at the elevation s , exhibiting deformation velocity v and thermal dilation k , $w(b_m)$ is the additive clutter and noise contribution to the m -th acquisition, and $\mathbf{a}(s, v, k)$ is the steering vector. Note that, after the above mentioned flat Earth removal operation, the elevation s is related to the height z by the relation $z = s \sin(\theta)$, where θ is the look angle introduced in Figure 1, so that the steering vector in Equation (4) is depending on look angle.

The presence of one scatterer can be verified by performing a statistical test. In Equation (3), the noise vector \mathbf{w} can be assumed as circularly symmetric complex (or proper complex) Gaussian vector, with uncorrelated samples and mutually uncorrelated real and imaginary parts, with zero-mean and same variance σ^2 . The probability density functions under the two hypotheses are both Gaussian, under $H_1, f_{H_1}(\mathbf{u}; \gamma, s, v, k, \sigma^2)$ depends on the target parameters (γ, s, v, k) and on the noise variance σ^2 , while under $H_0, f_{H_0}(\mathbf{u}; \sigma^2)$ depends only on the noise variance σ^2 . The two hypotheses can be identified applying a Generalized Likelihood Ratio Test (GLRT) [29]:

$$\Lambda = \frac{\max_{\gamma, s, v, k, \sigma^2} f_{H_1}(\mathbf{u}; \gamma, s, v, k, \sigma^2)}{\max_{\sigma^2} f_{H_0}(\mathbf{u}; \sigma^2)} \begin{matrix} > \\ < \end{matrix} \begin{matrix} H_1 \\ H_0 \end{matrix} \eta. \tag{5}$$

The threshold η is set using a Constant False Alarm Rate approach, which consists in imposing a false alarm rate equal to an assigned value, and evaluating the corresponding threshold by means of Monte Carlo simulation. A sample size of realizations (the size should be chosen in accordance with the fixed rate) of noise signals, i.e., the data under hypothesis H_0 is generated, and the threshold is evaluated such that the GLRT is over the threshold with the fixed false alarm rate.

The expression of the Maximum Likelihood estimates of γ and σ^2 maximizing Equation (5) can be found in a closed form. Consequently, after some mathematical manipulations, a simplified form of the test is obtained [36,37]:

$$\Lambda' = \frac{\max_{s, v, k} \frac{1}{M} |\mathbf{a}^H(s, v, k) \mathbf{u}|^2}{\mathbf{u}^H \mathbf{u}} \begin{matrix} > \\ < \end{matrix} \begin{matrix} H_1 \\ H_0 \end{matrix} \eta'. \tag{6}$$

The detector in Equation (6) exhibits performance, in terms of detection capabilities (for an assigned false alarm rate) and in terms of parameter estimation accuracy, that depends on the number of acquisitions M , on the scatterer coherence among the M acquisitions, and on the Signal to Noise Ratio (SNR). In practice, the performance can be unsatisfactory when M is too small [36,37]. Hence, to improve the performance achieved with a fixed false alarm, contextual information can improve the detector performance. For each considered pixel of the image, a patch of L pixels, typically a window of $N \times N$ pixels, with $L = N^2$ can be considered, so that the number of data exploited to detect the scatterer and estimate the corresponding parameters (s, v, k) is increased of a factor L . A common assumption, if N is limited, consists in assuming that the pixels belonging to the same patch exhibit the same target parameters, so that the test becomes a Multi-look test (MGLRT) [36,37]:

$$\Lambda_{ML} = \frac{\max_{s, v, k} \sum_{l=1}^L \frac{1}{M} |\mathbf{a}^H(s, v, k) \mathbf{u}_l|^2}{\sum_{l=1}^L \mathbf{u}_l^H \mathbf{u}_l} \begin{matrix} > \\ < \end{matrix} \begin{matrix} H_1 \\ H_0 \end{matrix} \eta_{ML}. \tag{7}$$

In this paper, the Test (7) is applied to recover the 5D reconstruction of the illuminated scene; where the target is present, it provides a reliable estimate of elevation, deformation velocity, and thermal expansion coefficient. The accuracy of the parameters' estimates is related to the scatterers' intensity and to their coherence over time: the higher the scatterer intensity and the temporal coherence, the more accurate the parameter estimation. The pixel neighborhood dimension L , for consideration in Test (7) is selected based on a compromise between estimation accuracy and the compliance of the assumption that all L pixels share the same parameter values. In this paper, a neighborhood with $L = 9$, considering 3×3 r - x cells for each pixel has been chosen (see [37] for details).

The procedure followed by MGLRT for the detection of a single scatterer is reported in Table 1:

Table 1. Procedure for the detection of a single scatterer in a pixel of the SAR image.

1.	Initialize $S = \{s_1, \dots, s_{N_s}\}$
2.	Initialize $V = \{v_1, \dots, v_{N_v}\}$
3.	Initialize $K = \{k_1, \dots, k_{N_k}\}$
4.	Select the patch of $N \times N$ pixels, with $L = N^2$
5.	For $s \in S, v \in V, k \in K$ compute $(\hat{s}, \hat{v}, \hat{k}) = \underset{s,v,k}{\operatorname{argmax}} \sum_{l=1}^L \frac{1}{M} a^H(s, v, k) u_l ^2$
6.	Compute $\Lambda_{ML} = \frac{\sum_{l=1}^L \frac{1}{M} a^H(\hat{s}, \hat{v}, \hat{k}) u_l ^2}{\sum_{l=1}^L u_l^H u_l}$
7.	if $\Lambda_{ML} > \eta_{ML}$
8.	decide for hypothesis H_1
9.	else
10.	decide for hypothesis H_0

In Table 1, the sets S , V , and K represent the range values for the triplet (s, v, k) , and the initialization is done considering a search grid for each parameter, compatible with the illuminated scene and the considered phenomena. For instance, in urban areas, where skyscrapers are present, the maximum elevation can be set to 150 m, the thermal dilation parameter depends on the material and can be set, at most, to 1 or 2 mm/°C, and the deformation average velocity can be set, at most, to 1 or 2 cm/year. The maximization in step 5 consists in an exhaustive search of the entire parameters' space.

3. Numerical Experiments on TSX Data

This section presents the experimental results on real data.

The experiments are carried out on SCL (single-look complex) StripMap TSX data. A stack of $M = 27$ azimuth-range focused TSX interferometric images is considered. The TSX system configuration parameters are presented in Table 2 and the orthogonal baselines in Table 3.

Table 2. TSX Configuration parameters.

Wavelength λ (m)	0.0311
View angle θ (°)	28.75
Range R_0 (km)	579.4
Number of images M	27
Total Baseline b_{TOT} (m)	751.6

Figure 2 shows the baselines' distribution for the considered TSX data, in Figure 2a the distribution of orthogonal versus temporal baselines; in Figure 2b, the distribution of temperature versus temporal baselines. The acquired images cover a period of 2 years and half, from May 2012 to November 2014, with an average time difference between two adjacent acquisitions of 27 days. The temperature is the daily averaged temperature of the illuminated scene, which has a seasonal behavior and varies from 7 °C to 33 °C. The average temperature difference between two consecutive acquisitions is ca. 1 °C. Indeed, the temperature distribution to be used in Equation (2) should be acquired on the analyzed structure, and at the acquisition time, but the choice of daily averaged temperature is reasonable and truly chosen [31–35]. Correlation between the temporal and temperature distributions should be limited, since it may affect the estimation of the deformation mean

velocity; in fact, ground deformation can be confused with seasonal deformation. In the considered TSX data, limited correlation is visible in Figure 2.

Table 3. TSX orthogonal baselines.

#	Orthogonal Baseline	#	Orthogonal Baseline
1	0	15	−226.36
2	−222.82	16	−92.59
3	42.88	17	−166.19
4	−248.09	18	−227.51
5	204.79	19	−71.75
6	180.81	20	−140.45
7	−144.09	21	308.98
8	−228.05	22	328.46
9	−121.66	23	375.41
10	−273.07	24	−314.94
11	79.31	25	436.66
12	200.11	26	206.31
13	−230.89	27	300.73
14	−100.77		

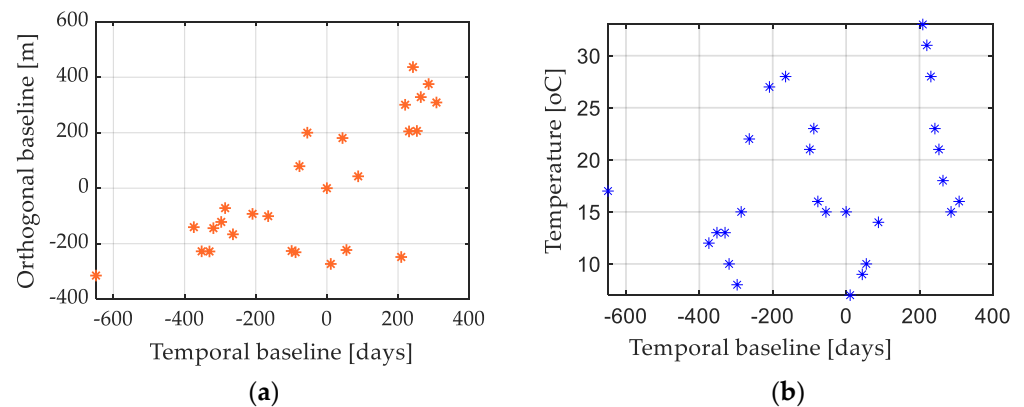


Figure 2. Baselines’ distribution for TSX data: (a) Distribution of orthogonal vs. temporal baselines; (b) Distribution of temperature versus temporal baselines.

4. Results and Discussion

Two different urban test sites in Naples (Italy) were considered:

- (1) an area around the Galleria Umberto I, which is a high and spacious cross-shaped structure, surmounted by a glass dome braced by 16 metal ribs, height 57 m, with four iron and glass-vaulted wings, maximum length 147 m, width 15 m, height 34.5 m;
- (2) an area around the Jolly Hotel, which is one of the tallest buildings in Naples, made of reinforced concrete, height 100 m, with a telecommunications tower on the top.

Figure 3 refers to the first site and shows the optical and SAR images of Galleria Umberto I and its neighborhood. The first thing to be noted is that a SAR image (Figure 3b) needs processing and interpretation for structure monitoring. In fact, SAR images undergo well-known geometric distortions, such as shadowing and layover [4], which are related to the slanted imaging coordinate system of the SAR sensor, causing the points at higher elevations to appear in the image at smaller range values. The layover effect will clearly appear in the reconstructed height maps, but can be easily compensated after height estimation, by means of the geocoding operation.

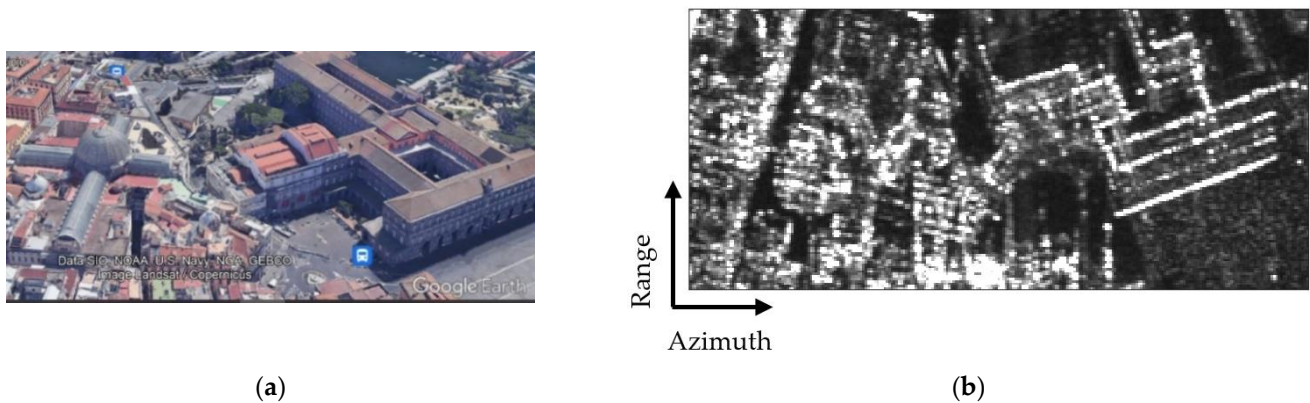


Figure 3. Images of Galleria Umberto I, Naples, Italy. (a) Optical image and (b) SAR image (Copyright DLR 2012–2014).

In Figure 4a–d, the LiDAR ground truth (a) and the height maps of the test site estimated using single-look GLRT (b) and MGLRT using 3×3 (c) and 5×5 (d) patches are presented. In the maps, only the height values of the scatterers with a value of Λ_{ML} greater than the fixed threshold (see Equation (7)) are shown. It can be easily noted that when increasing the patch size, the reconstructed height maps are more dense and less noisy, but spatial resolution decreases and some details are lost. A good compromise between scatterers' density and resolution is given by the results obtained using the 3×3 patch. In Figure 4b–d, we can also notice the phenomenon of layover, causing the point with high elevations to be located at lower range values. The reconstructed height map exhibits a satisfactory accuracy when compared with the LiDAR map (Figure 4a). For instance, the height of the dome is well estimated as ca. 60 m.

In Figure 5a, the MGLRT thermal dilation map which was obtained by applying a 3×3 patch is shown. In this map, a significant thermal dilation is present on the iron and glass dome and vaulted wings, as expected. In Figure 5b, MGLRT estimated a height map obtained without including thermal dilation and by applying a 3×3 patch is shown. By comparing the height map obtained in this case with the LiDAR one (Figure 4a) and with the one obtained by considering the thermal dilation (Figure 4c), it appears evident that this map is less accurate than the one obtained taking into account thermal dilation. In fact, in Figure 5b, the dome is not any more visible with its 60 m height. This behavior proves the importance of including this deformation component in the signal model.

In Figure 6a–c, the points were detected using MGLRT with a 3×3 patch, located in the optical 3D image, with a colorization corresponding to the height (a), to the deformation velocity (b), and to the thermal dilation coefficient (c) which are presented. A negligible deformation velocity can be appreciated, while thermal dilation coefficient is not negligible and is increasing with the height, as expected.

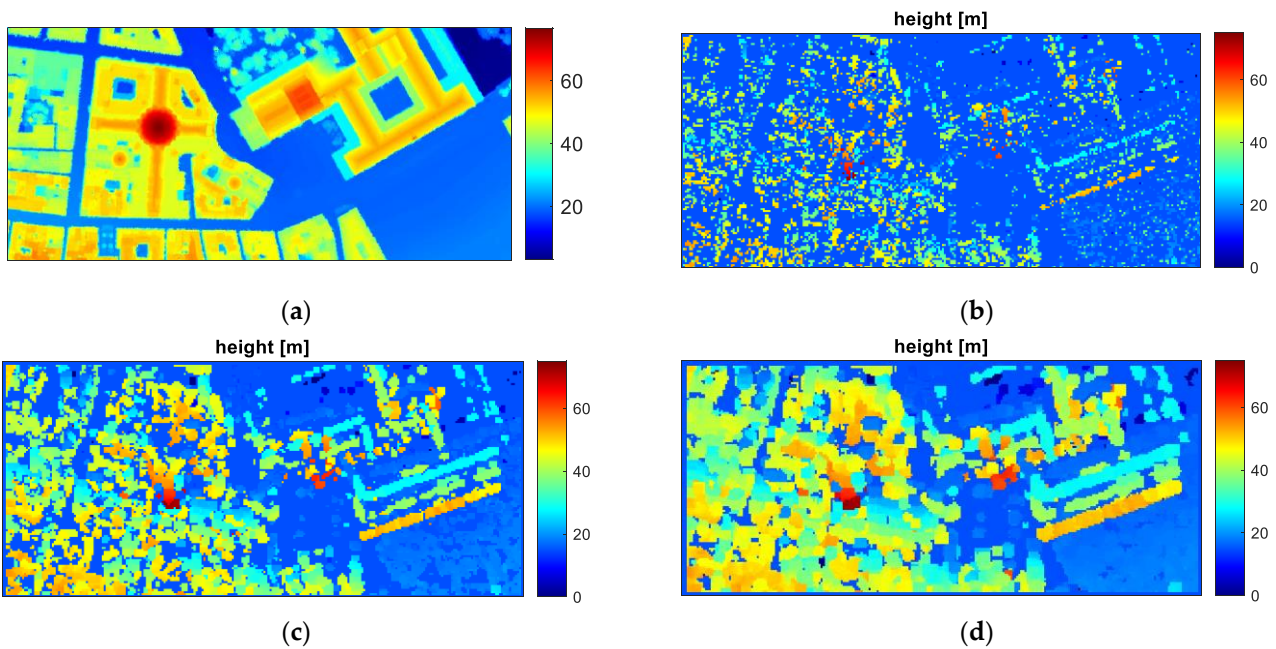


Figure 4. Galleria Umberto I test site: (a) LiDAR height map; (b) Single-look GLRT height map; (c) MGLRT height map obtained using a 3×3 patch; (d) MGLRT height map obtained using a 5×5 patch.

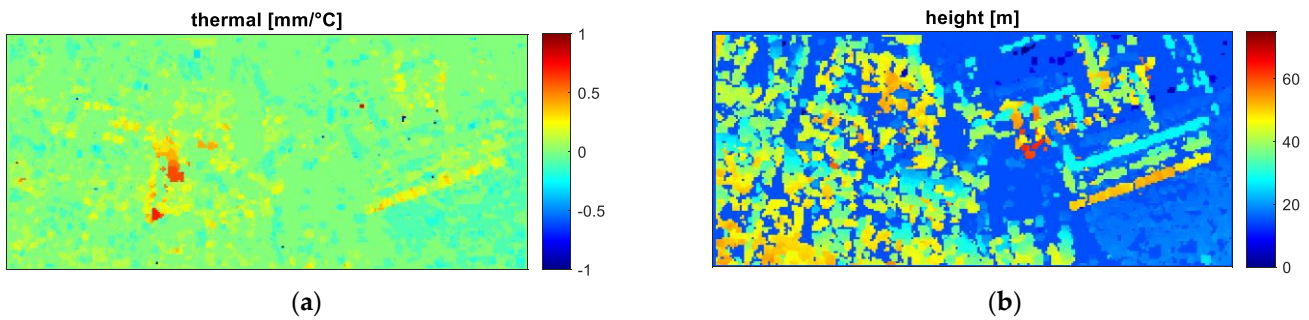


Figure 5. (a) MGLRT thermal dilation map with a 3×3 patch; (b) MGLRT height map with a 3×3 patch estimated without considering thermal dilation.

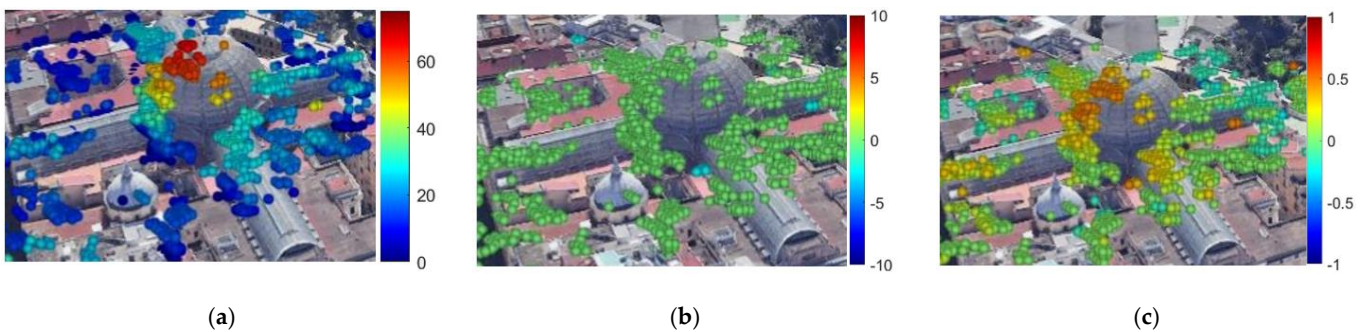


Figure 6. Galleria Umberto I test site: (a) points detected using MGLRT with a 3×3 patch, positioned in the optical 3D image, with a colorization corresponding to the height (m), (b) to the linear deformation velocity (mm/year), and (c) to the thermal dilation coefficient (mm/°C).

The thermal dilation map shows a positive trend with height. Positive values of the estimated thermal dilation coefficient indicate that a positive temperature difference produced a displacement toward the sensor. Construction materials expand when the

temperature increases, and this expansion is greater along the longest side of the geometric shape of the considered structure. This justifies why we estimate a greater thermal dilation coefficient on the top of the dome. The maximum thermal coefficient observed on the dome top is about $0.8 \text{ mm}/^\circ\text{C}$. The computation of the thermal expansion coefficient is complex, due to the geometry of the dome; as reported in Section 2, it takes into account the percentage change in structure length, per degree of temperature change. The obtained result shows that the maximum thermal dilation coefficient estimated is of the order of magnitude of the thermal coefficient of iron (about $12 \times 10^{-6} \text{ (m)/(m}\cdot^\circ\text{C)}$); in fact, considering the maximum height of the dome (57 m), the thermal expansion is about $8 \times 10^{-4}/57 = 14 \times 10^{-6} \text{ (m)/(m}\cdot^\circ\text{C)}$.

Figure 7 refers to the second test site and shows the optical and SAR images of Jolly Hotel and its neighborhood. Since this building is very tall (about 100 m), the layover effect is quite visible. In Figure 8a–d, the LiDAR ground truth (a) and the height maps of the test site estimated using single-look GLRT (b) and MGLRT using 3×3 (c) and 5×5 (d) patches are presented. Additionally, in this case, the 3×3 patch represents a good compromise between resolution and accuracy. In Figure 8b–d, the layover effect is quite evident, since the top of the tall building corresponds in the SAR image and in the corresponding height map to a smaller slant range than that of its bottom. Moreover, the height of the building is well estimated at about 100 m.

In this experiment, again, no linear deformation velocity has been detected, but the thermal dilation effect is visible in the map shown in Figure 9a. It is very clear in Figure 9b that without considering the thermal contribution, the height reconstruction fails, since the top of the building is not visible. Then, it is not possible to find critical points on the top for monitoring the structure. Finally, we show the detected cloud points relocated on the structure in the optical 3D image in Figure 10. Again, a positive thermal dilation coefficient increasing with the height, as expected, is reported in Figure 10b. The maximum thermal expansion that is observed on the top is about $0.9 \text{ mm}/^\circ\text{C}$, so that, considering the building height of 100 m, the thermal expansion is about $9 \times 10^{-4}/100 = 9 \times 10^{-6} \text{ m/(m}\cdot^\circ\text{C)}$, which is compatible with the thermal expansion coefficient of the concrete (about $10 \times 10^{-6} \text{ (m)/(m}\cdot^\circ\text{C)}$).

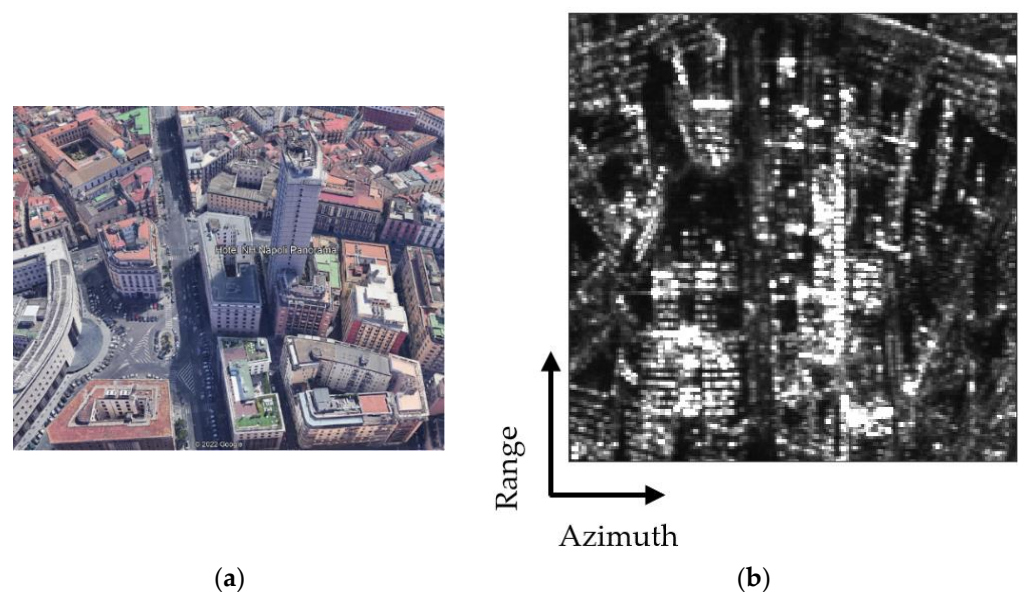


Figure 7. Images of Jolly Hotel, Naples, Italy. (a) Optical image and (b) SAR image (Copyright DLR 2012–2014).

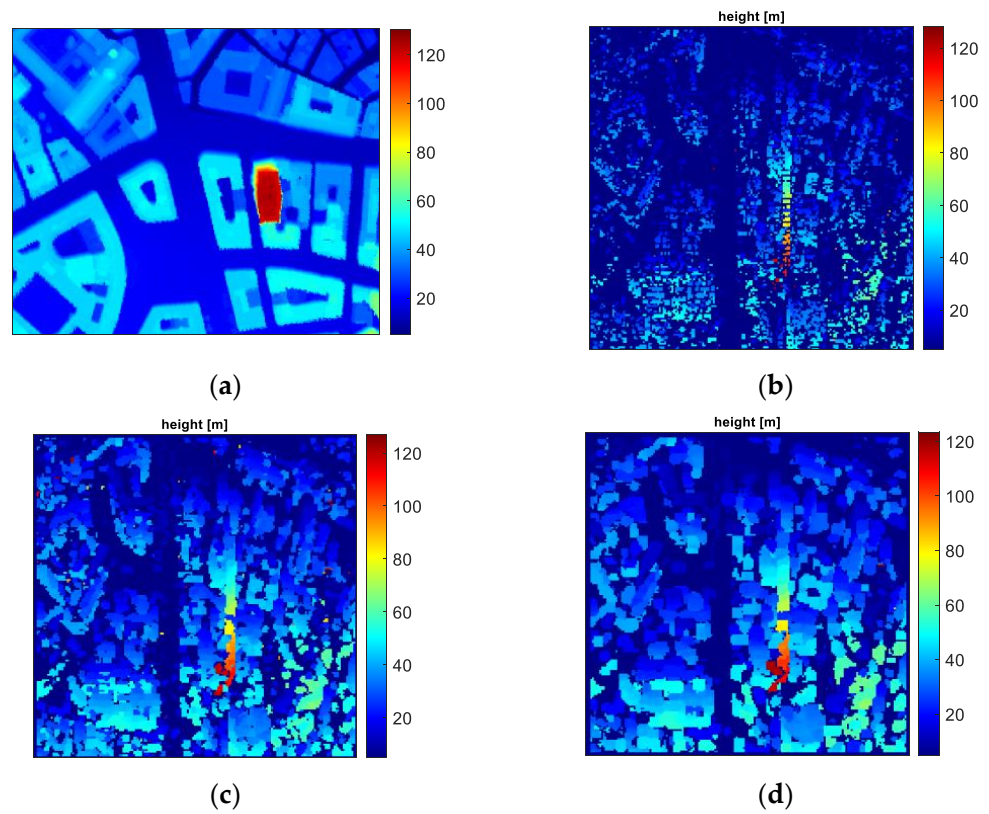


Figure 8. Jolly Hotel test site: (a) LiDAR height map; (b) Single-look GLRT height map; (c) MGLRT height map obtained using a 3×3 patch; (d) MGLRT height map obtained using a 5×5 patch.

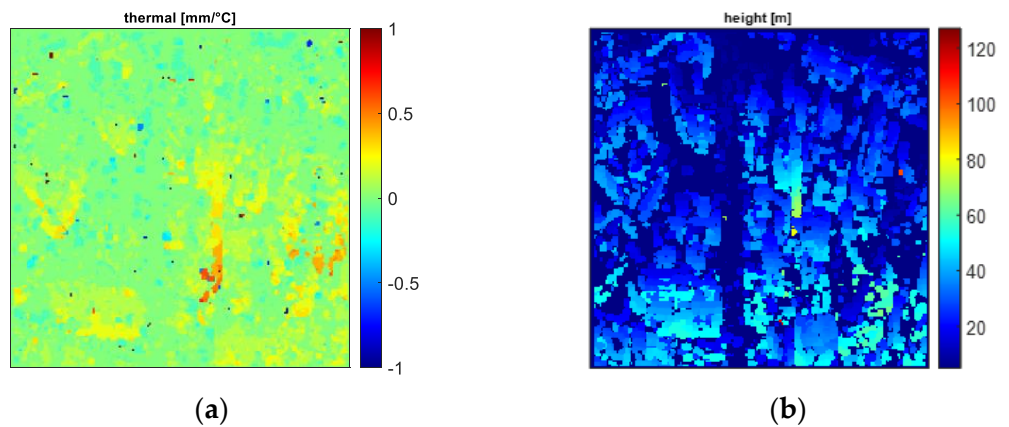


Figure 9. (a) MGLRT thermal dilation map with a patch 3×3 , (b) MGLRT height map with a patch 3×3 without considering thermal dilation.

The results presented demonstrate that the adopted TomoSAR technique applied on TSX data exhibits a good capability of computing the height profile of structures on the ground and allows the estimation of their deformations on a sub-centimeter scale, separating thermal dilation from other kinds of temporal deformations.

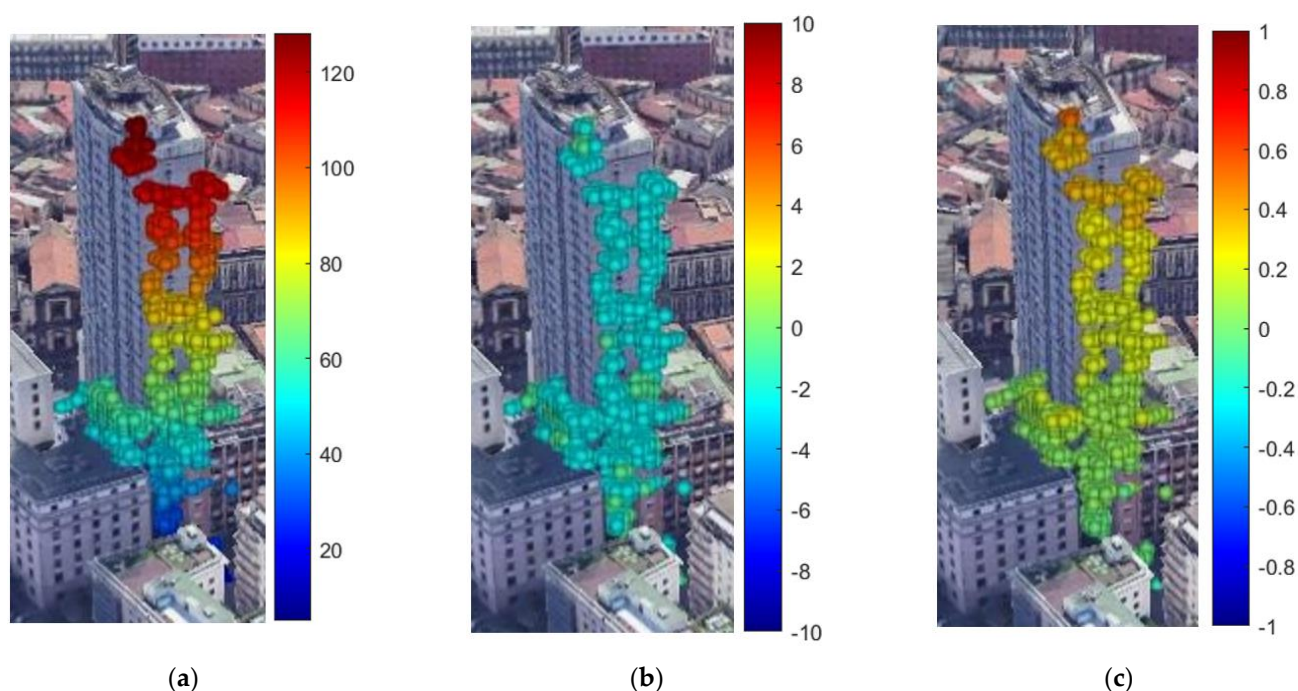


Figure 10. Jolly Hotel test site: (a) points detected using MGLRT with a 3×3 patch, positioned in the optical 3D image, with a colorization corresponding to the height (m), (b) to the linear deformation velocity (mm/year), and (c) to the thermal dilation coefficient (mm/°C).

5. Conclusions

In this paper, we show that SAR tomography can be a useful technique for civil structure health monitoring. A stack of SAR images of the structure under monitoring acquired during the observation period are needed, but the cost would be significantly lower than that of in situ contact sensors and ground investigation. The choice of the sensor depends on the availability of the data, but also on the systems characteristics required, such as revisiting time, spatial resolution, and wavelength, which is related to the sensor sensitivity and consequently, to the spatial scale of the movements that need to be monitored.

A Multi-look GLRT-based SAR tomographic technique has been applied. It exploits context information, processing image patches instead of pixel by pixel, achieving a better estimation accuracy. The adopted approach is able to estimate the height and two components of temporal displacements at a millimeter scale: a deformation component linear with time, which is usually related to presence of subsidence and structural damages, and a displacement component linear with the temperature, which is related to the thermal dilation effect of solid structures.

It has been shown that if the thermal dilation contribution is not taken into account in the model and not estimated, the assumption of the only linear deformation contribution can lead to not reliable estimates of the structure height and corresponding possible deformation. We note that this achievement has been reached considering an X-band SAR system (high sensitivity), and assuming for the thermal contribution the simplest possible model, linear with temperature. Of course, a more sophisticated model will certainly ensure better thermal dilation estimates, but the investigation of a more complex model is beyond the aim of the paper.

Applying the detection test, the more reliable points can be identified by means of a fixed constant false alarm criterion, and the estimated displacements on these points can be, then, usefully employed for the structure health monitoring. The high scatterers' density obtained is due to the coherent processing in the elevation direction, typical of TomoSAR

and not performed in InSAR techniques. The proposed approach allows to increase the signal to clutter ratio in the focused 3D domain also thanks to the multi-looking procedure.

In the numerical experiments, it has been discussed the dimension of the patch that should be considered for the multi-looking; the experiments on real TSX data have proven that a 3×3 is a good choice with a slight loss in resolution but a gain in accuracy. The only assumption that has to be done about the monitored structure is that the resolution of SAR system is such that the structure size is compatible with the chosen patch.

Finally, it should be highlighted that the presented work aims to show the potential of a TomoSAR approach in SHM, focusing on the scatterers' density and the reliability of the parameters' estimates (height, thermal dilation, deformation), but it is still not ready for being utilized by the industry. Limitations are the simple thermal dilation model, as discussed, and the lack of a consolidated procedure that helps the user to detect an anomalous behavior that can candidate a structure as a potentially damaged one, a type of damage index.

Author Contributions: A.B. and G.S.; Data curation, A.B. and G.S.; Methodology, A.B. and G.S.; Writing—original draft, A.B. and G.S. All the authors contributed in all aspects of this work. All authors have read and agreed to the published version of the manuscript.

Funding: This research received no external funding.

Informed Consent Statement: Not applicable.

Data Availability Statement: Not applicable.

Acknowledgments: We thank the DLR for providing data.

Conflicts of Interest: The authors declare no conflict of interest.

References

1. Kralovec, C.; Schagerl, M. Review of Structural Health Monitoring Methods Regarding a Multi-Sensor Approach for Damage Assessment of Metal and Composite Structures. *Sensors* **2020**, *20*, 826. [[CrossRef](#)] [[PubMed](#)]
2. Yarnold, M.T.; Moon, F. Temperature-based structural identification of long-span bridges. *J. Struct. Eng.* **2015**, *141*, 04015027. [[CrossRef](#)]
3. Reilly, J.; Glisic, B. Identifying Time Periods of Minimal Thermal Gradient for Temperature-Driven Structural Health Monitoring. *Sensors* **2018**, *18*, 734. [[CrossRef](#)] [[PubMed](#)]
4. Fornaro, G.; Pascazio, V. SAR Interferometry and Tomography: Theory and Applications. Academic Press Library in Signal Processing. In *Communications and Radar Signal Processing*, 2nd ed.; Elsevier Ltd.: Amsterdam, The Netherlands, 2013; pp. 1043–1117.
5. DePrekel, K.; Bouali, E.H.; Oommen, T. Monitoring the Impact of Groundwater Pumping on Infrastructure Using Geographic Information System (GIS) and Persistent Scatterer Interferometry (PSI). *Infrastructures* **2018**, *3*, 57. [[CrossRef](#)]
6. Gabriel, A.K.; Goldstein, R.M.; Zebker, H.A. Mapping small elevation changes over large areas: Differential radar interferometry. *J. Geophys. Res.* **1989**, *94*, 9183–9191. [[CrossRef](#)]
7. Ferretti, A.; Prati, C.; Rocca, F. Nonlinear subsidence rate estimation using permanent scatterers in differential SAR interferometry. *IEEE Trans. Geosci. Remote Sens.* **2000**, *38*, 2202–2212. [[CrossRef](#)]
8. Berardino, P.; Fornaro, G.; Lanari, R.; Sansosti, E. A new algorithm for surface deformation monitoring based on small baseline differential sar interferograms. *IEEE Trans. Geosci. Remote Sens.* **2002**, *40*, 2375–2383. [[CrossRef](#)]
9. Gernhardt, S.; Adam, N.; Eineder, M.; Bamler, R. Potential of very high resolution SAR for persistent scatterer interferometry in urban areas. *Ann. GIS* **2000**, *16*, 103–111. [[CrossRef](#)]
10. Ferretti, A.; Prati, C.; Rocca, F. Permanent scatterers in SAR interferometry. *IEEE Trans. Geosci. Remote Sens.* **2001**, *39*, 8–20. [[CrossRef](#)]
11. Crosetto, M.; Monserrat, O.; Iglesias, R.; Crippa, B. Persistent scatterer interferometry: Potential, limits and initial C- and X-band comparison. *Photogramm. Eng. Remote Sens.* **2010**, *76*, 1061–1069. [[CrossRef](#)]
12. Lan, H.; Li, P.; Liu, H.; Yang, Z. Complex urban infrastructures deformation monitoring using high resolution PSI. *IEEE J. Sel. Top. Appl. Earth Obs. Remote Sens.* **2012**, *5*, 643–651. [[CrossRef](#)]
13. Crosetto, M.; Monserrat, O.; Cuevas-Gonzalez, M.; Devanthery, N.; Luzi, G.; Crippa, B. Measuring thermal expansion using X-band persistent scatterer interferometry. *ISPRS J. Photogramm. Remote Sens.* **2015**, *100*, 84–91. [[CrossRef](#)]
14. Monserrat, O.; Crosetto, M.; Cuevas, M.; Crippa, B. The thermal expansion component of Persistent Scatterer Interferometry observations. *IEEE Geosci. Remote Sens. Lett.* **2011**, *8*, 864–868. [[CrossRef](#)]

15. Lazecky, M.; Hlavacova, I.; Bakon, M.; Sousa, J.; Perissin, D.; Patricio, G. Bridge displacements monitoring using space-borne X-band SAR interferometry. *IEEE J. Sel. Top. Appl. Earth Obs. Remote Sens.* **2017**, *10*, 205–210. [[CrossRef](#)]
16. Qin, X.; Liao, M.; Zhang, L.; Yang, M. Structural health and stability assessment of high-speed railways via thermal dilation mapping with time-series InSAR analysis. *IEEE J. Sel. Top. Appl. Earth Obs. Remote Sens.* **2017**, *10*, 2999–3010. [[CrossRef](#)]
17. Jung, J.; Kim, D.-j.; Palanisamy Vadivel, S.K.; Yun, S.-H. Long-Term Deflection Monitoring for Bridges Using X and C-Band Time-Series SAR Interferometry. *Remote Sens.* **2019**, *11*, 1258. [[CrossRef](#)]
18. Wang, Z.; Liu, M. Seasonal Deformation and Accelerated Motion of Infrastructure Monitoring Using a Generalized Differential SAR Tomography. *IEEE Geosci. Remote Sens. Lett.* **2020**, *17*, 626–630. [[CrossRef](#)]
19. Yang, B.; Xu, H.; Jiang, L.; Huang, R.; Zhou, Z.; Wang, H.; Liu, W. A Multicomponent Temporal Coherence Model for 3-D Phase Unwrapping in Time-Series InSAR of Seasonal Deformation Areas. *Remote Sens.* **2022**, *14*, 1080. [[CrossRef](#)]
20. Reigber, A.; Moreira, A. First Demonstration of Airborne SAR Tomography Using Multibaseline L-band Data. *IEEE Trans. Geosci. Remote Sens.* **2000**, *38*, 2142–2152. [[CrossRef](#)]
21. Budillon, A.; Crosetto, M.; Johnsy, A.C.; Monserrat, O.; Krishnakumar, V.; Schirinzi, G. Comparison of Persistent Scatterer Interferometry and SAR Tomography Using Sentinel-1 in Urban Environment. *Remote Sens.* **2018**, *10*, 1986. [[CrossRef](#)]
22. Lombardini, F. Differential tomography: A new framework for SAR interferometry. *IEEE Trans. Geosci. Remote Sens.* **2005**, *43*, 37–44. [[CrossRef](#)]
23. Fornaro, G.; Lombardini, F.; Serafino, F. Three-Dimensional Multipass SAR Focusing: Experiments with Long-Term Spaceborne Data. *IEEE Trans. Geosci. Remote Sens.* **2005**, *40*, 702–714. [[CrossRef](#)]
24. Budillon, A.; Evangelista, A.; Schirinzi, G. Three-Dimensional SAR Focusing from Multipass Signals Using Compressive Sampling. *IEEE Trans. Geosci. Remote Sens.* **2011**, *49*, 488–499. [[CrossRef](#)]
25. Zhu, X.X.; Bamler, R. Super-Resolution Power and Robustness of Compressive Sensing for Spectral Estimation with Application to Spaceborne Tomographic SAR. *IEEE Trans. Geosci. Remote Sens.* **2012**, *50*, 247–258. [[CrossRef](#)]
26. Budillon, A.; Ferraioli, G.; Schirinzi, G. Localization Performance of Multiple Scatterers in Compressive Sampling SAR Tomography: Results on COSMO-SkyMed Data. *IEEE J. Sel. Top. Appl. Earth Obs. Remote Sens.* **2014**, *7*, 2902–2910. [[CrossRef](#)]
27. Pauciuлло, A.; Reale, D.; De Maio, A.; Fornaro, G. Detection of Double Scatterers in SAR Tomography. *IEEE Trans. Geosci. Remote Sens.* **2012**, *50*, 3567–3586. [[CrossRef](#)]
28. Budillon, A.; Schirinzi, G. GLRT Based on Support Estimation for Multiple Scatterers Detection in SAR Tomography. *IEEE J. Sel. Top. Appl. Earth Obs. Remote Sens.* **2016**, *9*, 1086–1094. [[CrossRef](#)]
29. Budillon, A.; Johnsy, A.; Schirinzi, G. A Fast support detector for superresolution localization of multiple scatterers in SAR tomography. *IEEE J. Selected Topics Appl. Earth Obs. Remote Sens.* **2017**, *10*, 2768–2779. [[CrossRef](#)]
30. Budillon, A.; Johnsy, A.; Schirinzi, G. Urban Tomographic Imaging Using Polarimetric SAR Data. *Remote Sens.* **2019**, *11*, 132. [[CrossRef](#)]
31. Fornaro, G.; Serafino, F.; Reale, D. 4D SAR imaging for height estimation and monitoring of single and double scatterers. *IEEE Trans. Geosci. Remote Sens.* **2009**, *47*, 224–237. [[CrossRef](#)]
32. Fornaro, G.; Reale, D.; Verde, S. Bridge thermal dilation monitoring with millimeter sensitivity via multidimensional SAR imaging. *IEEE Geosci. Remote Sens. Lett.* **2013**, *10*, 677–681. [[CrossRef](#)]
33. Reale, D.; Fornaro, G.; Pauciuлло, A. Extension of 4-D SAR imaging to the monitoring of thermally dilating scatterers. *IEEE Geosci. Remote Sens. Lett.* **2013**, *51*, 5296–5306. [[CrossRef](#)]
34. Budillon, A.; Johnsy, A.; Schirinzi, G. Extension of a fast GLRT algorithm to 5D SAR tomography of Urban area. *Remote Sens.* **2017**, *9*, 844. [[CrossRef](#)]
35. Rambour, C.; Budillon, A.; Johnsy, A.C.; Denis, L.; Tupin, F.; Schirinzi, G. From Interferometric to Tomographic SAR: A Review of Synthetic Aperture Radar Tomography-Processing Techniques for Scatterer Unmixing in Urban Areas. *IEEE Geosci. Remote Sens. Mag.* **2020**, *8*, 6–29. [[CrossRef](#)]
36. Pauciuлло, A.; Reale, D.; Franzé, W.; Fornaro, G. Multi-look in GLRT-based detection of single and double persistent scatterers. *IEEE Trans. Geosci. Remote Sens.* **2018**, *56*, 5125–5137. [[CrossRef](#)]
37. Liu, W.; Budillon, A.; Pascazio, V.; Schirinzi, G.; Xing, M. Performance Improvement for SAR Tomography Based on Local Plane Model. *IEEE J. Selected Topics Appl. Earth Obs. Remote Sens.* **2022**, *15*, 2298–2310. [[CrossRef](#)]
38. Ho, C.Y.; Taylor, R.E. *Thermal Expansion of Solids*; ASM International: Materials Park, OH, USA, 1998.